Mapping the Partial Shading Degradation in a Monolithically Integrated Perovskite Module

Aninat, Remi; Bakker, Klaas; Henzel, Jonathan; Zardetto, Valerio; Dogan, Ilker; Gevaerts, Veronique; Veenstra, Sjoerd; Theelen, Mirjam

DOI
10.1002/pip.3881

Publication date
2025

Document Version
Final published version

Published in
Progress in Photovoltaics: research and applications

Citation (APA)
Aninat, R., Bakker, K., Henzel, J., Zardetto, V., Dogan, I., Gevaerts, V., Veenstra, S., & Theelen, M. (2025). Mapping the Partial Shading Degradation in a Monolithically Integrated Perovskite Module. *Progress in Photovoltaics: research and applications*, *34*(1), 60-68. https://doi.org/10.1002/pip.3881

Progress in Photovoltaics: Research and Applications

WILEY

PROGRESS IN PHOTOVOLTAICS

SPECIAL ISSUE ARTICLE

Mapping the Partial Shading Degradation in a Monolithically Integrated Perovskite Module

Remi Aninat[1] | Klaas Bakker[1] | Jonathan Henzel[1,2] | Valerio Zardetto[1] | Ilker Dogan[1] | Veronique Gevaerts[1] | Sjoerd Veenstra[1] | Mirjam Theelen[1]

[1]Solar Technologies and Applications, TNO, Eindhoven, The Netherlands | [2]Photovoltaic Materials and Devices, Delft University of Technology, Delft, The Netherlands

Correspondence: Remi Aninat (remi.aninat@tno.nl)

Received: 28 June 2024 | **Revised:** 2 December 2024 | **Accepted:** 5 December 2024

Funding: This work received funding from the Ministry of Economic Affairs and Climate Policy through the TNO Knowledge Investment Project (KIP).

Keywords: lock-in thermography | luminescence | mapping | module | partial shading | perovskite | reverse bias

ABSTRACT

Among reliability studies on perovskite photovoltaics (PV) cells and modules, partial shading degradation is a crucial and under-investigated topic. In the present work, we use a combination of mapping electroluminescence (EL), photoluminescence (PL), and illuminated lock-in thermography (ILIT) to gain insight into the reverse bias degradation mechanisms induced by partial shading on a monolithically interconnected module. Spatial inhomogeneities across the cell length are shown to play an important role in the degradation. A perovskite module was subjected to partial shading, causing, in the lower region of the shaded cells, a PL signal intensity increase and EL decrease. We suggest the formation of a barrier at one of the perovskite/transport layer interfaces, preventing both carrier extraction in PL and carrier injection in EL. A simple model for the current flow in the presence of the barrier can satisfactorily explain the EL, PL, and ILIT behavior and point to some possible propagation mechanisms. In summary, we show that studying partial shading degradation at module level draws a more complex and realistic picture of the interplay between material and electrical parameters than cell-level studies. We also demonstrate that luminescent and thermal imaging techniques can be combined to draw meaningful conclusions on the degradation mechanisms, their formation, and propagation.

1 | Introduction

Perovskite-based solar cells (PSC) are an emerging and promising technology. In single junction devices, they have achieved spectacular progress in the past few years, with a 26.1% efficiency record cell most recently [1]. Additionally, they are ideally suited to multijunction devices, where the wide bandgap of perovskite can be used as top cell in tandem with silicon [2] or CIGS [3]. Finally, its bandgap can be tuned to build fully perovskite tandem devices [4]. Being a thin-film technology, with the possibility of solution processing, it could potentially lead to low CAPEX and OPEX in large-scale production [5], boosting its scalability prospects. However, as for any PV technology, ensuring reliability is key to industrialization. The most studied reliability aspects of PSC are their resilience to heat, humidity, and UV exposure [6, 7].

However, partial shading is also a realistic threat to PV modules, which, unlike UV and water, cannot be mitigated by proper packaging and should therefore be considered in reliability studies [6, 8–10]. Partial shading frequently occurs outdoor when elements in the environment (e.g., tree branches, buildings, etc.) cast shading patterns onto solar modules. When, in a module, some cells in a string generate less current than others due to partial shading, a reverse bias can be induced in those shaded cells. The induced reverse bias can, in turn, cause lasting power conversion efficiency (PCE) degradation.

The electrical reverse bias behavior of a perovskite solar cell is characterized by a sudden increase in current at the breakdown voltage, similar to an avalanche or Zener diode. Unlike silicon solar cells, where breakdown is caused by the so-called "avalanche breakdown mechanism" [11], it is likely a tunnelling mechanism that is responsible for the breakdown in perovskite solar cells because the breakdown occurs at significantly lower voltages than in silicon. We found in the past that the breakdown voltage of a 1.6-eV bandgap PSC can be approximated as 2.5*Eg/q [12]. In Si and Ge homojunction devices, breakdown due to tunnelling appears at voltages below 4*Eg/q, and avalanche breakdown occurs at voltages above 6*Eg/q [13]. At the time of writing, the commonly accepted tunnelling mechanism for perovskite devices is given by Bowring et al. [14]. They proposed that upon reverse bias, ions migrate towards the interface between a charge transport layer and the perovskite. This, in turn, causes narrowing of the tunneling barrier width and facilitates tunnelling.

Concerning the degradation induced by reverse bias, various mechanisms have been proposed. First, fast and severe degradation can result from the formation of shunts, due to either migration of metal ions from the electrode or decomposition of the perovskite into conductive phases [14, 15]. This mechanism is somehow similar to the metallic phases typically forming in inorganic thin film technologies like CIGS [16, 17]. However, ion migration is central to the reverse bias behavior of perovskite, which is, to our knowledge, not the case in inorganic PV. For example, Razera et al. found that iodide can migrate into the organic electron transport layer (ETL) and create a barrier for charge transport [15, 18]. More interfacial processes, like dipole formation or defect accumulation, have also been proposed [14, 19]. In the bulk, halide ions can be oxidized, creating recombination centers [19], or segregate [15, 20]. For the segregation mechanisms, but also for other proposed mechanisms that consist of a redox reaction, the reverse bias current flow is assumed to be the driving force behind the degradation. According to Henzel et al., the loss of efficiency increases with the reverse bias current flow, which implies that these current-driven mechanisms dominate reverse bias degradation [21, 22]. However, most of the studies mentioned above are carried out by applying a reverse bias on individual cells. Although such an approach allows for a more in-depth study of the fundamental mechanisms, it does not account for all the processes that occur during the partial shading of a module. Single solar cells studied in the lab differ from cells in PV modules, especially monolithically interconnected ones, in various important respects. First, the presence of material inhomogeneities within large cells and across the module is more likely. These inhomogeneities might not impact the device properties in any significant way under standard test conditions but may locally affect the electrical properties, assisting defect formation in reverse bias and/or steering their propagation. Another difference between modules and cells is the presence of scribes and interconnects in modules, which can also affect the current distribution and pathways, hence the defect formation and propagation.

Monolithically interconnected cells, which is the dominant configuration in thin film modules, do not easily allow for the reverse bias mitigation methods normally implemented in other configurations, such as bypass diodes and parallel connection (see, e.g., Baumann et al. [10]). Instead, more innovative approaches such as shade tolerant cell designs [23] should be developed.

In the present work, two sets of experiments on two types of samples are presented. First, a full $100\times100\,mm^2$ (aperture area) module with monolithic, laser-scribed interconnection (initial efficiency of 15%), before and after degradation by partial shading, is characterized electrically and using various imaging techniques. The aim is to study the spatial homogeneity of the degradation.

In the second part, in order to help us interpret the results obtained on the module, data acquired on individual cells (i.e., breakdown voltage distribution and curves), made on a similar sample plate, are also analyzed.

The aim of this paper is to assess what information can be gained from imaging techniques such as photoluminescence (PL), electroluminescence (EL), and illuminated lock-in thermography (ILIT), especially regarding defect homogeneity and formation mechanism.

2 | Experimental

2.1 | Devices Fabrication

The module used in this study was processed on 6″ ($\approx152\times152\,mm^2$) glass substrates. The module has a PIN architecture with semi-transparent electrodes, where the cells are monolithically interconnected. The aperture area is $100\times100\,mm^2$ with a geometric fill factor of 92.5%. A 120-nm ITO layer was sputtered on a 1.1-mm-thick glass substrate, followed by sheet-to-sheet (S2S) slot-die deposition of a surface-modified poly(triaryl amine) (PTAA) hole transport layer (HTL). A 600-nm-thick $Cs_{0.05}FA_{0.81}MA_{0.14}PbI_{2.7}Br_{0.3}$ (+1 mol% RbCl) perovskite absorber layer ($Eg\approx1.6\,eV$) with phenethylammonium iodide salts (PEAI) passivation layers were slot-die coated on top of the HTL. The ETL, a 24-nm-thick C_{60} layer, was then evaporated, followed by spatial atomic layer deposition (sALD) of a 40-nm SnO_2 layer. The stack was finalized by DC sputtering of a 180-nm ITO layer. After fabrication, the modules are provided with current collecting tabs and encapsulated with an encapsulant and glass front sheet. A module consists of 31 cells that are monolithically interconnected by laser using a P1, P2, and P3 scribing process. Additionally, an isolation scribe was applied around the active area. The P1, P2, P3, and isolation scribes were applied using a 532-nm ps laser in N_2 atmosphere in a glove box with integrated filtering for safe processing of the perovskite material.

The smaller, individual cells were manufactured in a similar way to the module, using a S2S slot-die coater, on a $6\times6\,in.^2$ glass plate with patterned ITO. However, a metal grid was deposited at the top ITO side, for improved current collection, and the glass plate was subsequently cut into sixteen $30\times30\,mm^2$ substrates with four $4\times4\,mm^2$ cells on each. The cell area is defined by the overlap of the top and bottom ITO electrodes.

2.2 | Characterization Equipment and Settings

For the reverse bias current density-voltage (*JV*) sweep of the individual cells, an Autolab PGSTAT 30 controlled with the NOVA 2.1 software was used. A single cyclic voltammetry (*CV*) staircase

profile was applied, with a start and stop potential of 0 V, upper and lower vertex potentials of 1.2 and −8 V, scan rate of 200 mV/s, and a step of −10 mV; the limit for current density was set to 20 mA/cm^2. As reported in the literature [14, 15], the metal from the grids can cause shunts or defects to form during the reverse bias *CV* scan. The cells where this occurred were filtered out, resulting in a yield of 84%.

Note that for individual cells, we use *JV*, since current density allows for easier comparison between cells. For the module on the other hand, we will use "*IV*," since the aperture area includes several series-connected cells.

The dark and illuminated *IV* measurements on the module were carried out in a Neonsee AAA solar simulator using a Xenon lamp, under 1000 W/m^2 simulated AM1.5G illumination. The temperature was maintained at 23°C on a temperature-controlled vacuum chuck. The hysteresis sweep was started at 36 V, scanned down to −4 V, and then back up again to 36 V, with a 200-mV step size and a ≈1 V/s scan speed.

The ILIT measurements used a PV-LIT setup by InfraTec GmbH. The setup consists of a cooled indium-antimonide (InSb) infrared detector array and two green (522 nm) LED arrays. The lock-in frequency used was 0.1 Hz and the duration of the measurement 25 periods.

EL and PL were carried out in a LumiSolarCell system from GreatEyes, using a silicon CCD camera with a longpass filter cutting off around 750 nm. For EL, the power supply was a Keithley 2400 Source Measure Unit and the injected current 60 mA. The excitation source for the PL was a green (530 nm) LED array.

2.3 | Degradation Experiments

2.3.1 | Module Partial Shading

For the partial shading experiments (PSE), a fixed protocol was applied to a single module, summarized in Figure 1. A preconditioning step, consisting of one illuminated current–voltage (IV) measurement, followed by 2 min of maximum power point tracking at 1 sun illumination from each side, was applied on the module once at the beginning before going through the characterization/partial shading cycles. Note that in the very first cycle, dark and illuminated IV before the first partial shading stress applied to this module, PSE-A, were reversed.

To apply the partial shading stress, three adjacent cells of the module were fully covered with a 100% opaque mask. The optimal size for the mask was determined in a separate experiment. It was based on the criteria defined by IEC 61215-2 and Hermann et al. [24], with, however, an increased mask size, since we aimed for a maximum amount of current (I_{SC}) flowing through the shaded cells (see Figure S1). We chose to apply a reverse bias current close to I_{sc} to maximize the power dissipated in the shaded cells, thus accelerating the degradation. This condition is harsher than the more realistic scenario where a single module in a string is partially shaded, and the current does not exceed the maximum power point current.

Three different partial shading experiments were carried out sequentially on the module (PSE-A, PSE-B, and PSE-C), each shading a different group of cells, as illustrated in Figure 2. For the partial shading stress presented in this paper (PSE-C), which was the last and harshest of the three, the module was masked and placed onto a water-cooled (23°C) brass vacuum chuck and exposed to 1-sun illumination for 2 min in short circuit conditions. PSE-A and PSE-B (see details in Figure 2) were applied in a similar way, and although they induced similar PL and EL features to PSE-C (see Figure S2), they caused less degradation (because the shading was shorter and not at I_{SC}) and will therefore not be discussed further here.

We emphasize that the degradation observed in this specific module has occurred in other modules as well (e.g., the module used for mask size determination), yielding similar features. This indicates that partial shading is relevant to perovskite modules in general and should be seriously considered and tested for.

2.3.2 | Reverse Bias on Individual Cells

The reverse bias scans of the individual cells were performed 1 week after the illuminated forward scans. During this week, they were stored in the dark in an inert (N_2) atmosphere.

The negative voltage where the breakdown occurs (V_{BD}) is determined by measuring an extended range dark JV measurement. An example of such an extended dark *JV* curve is shown in

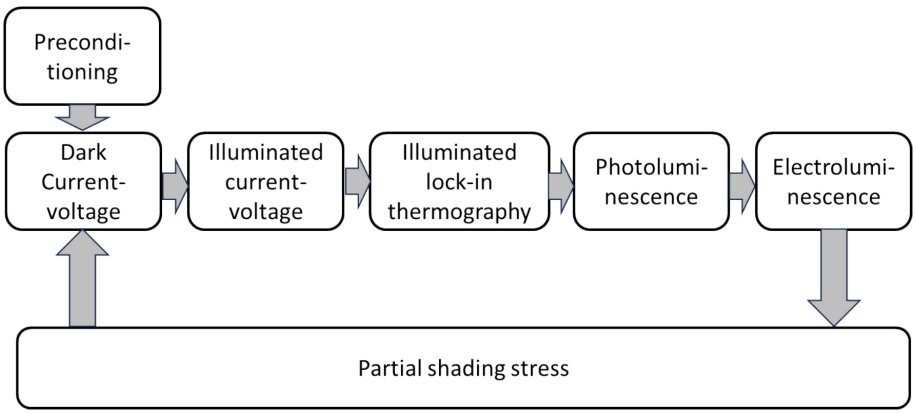

FIGURE 1 | Schematic illustrating the experimental protocol for the monolithically interconnected module.

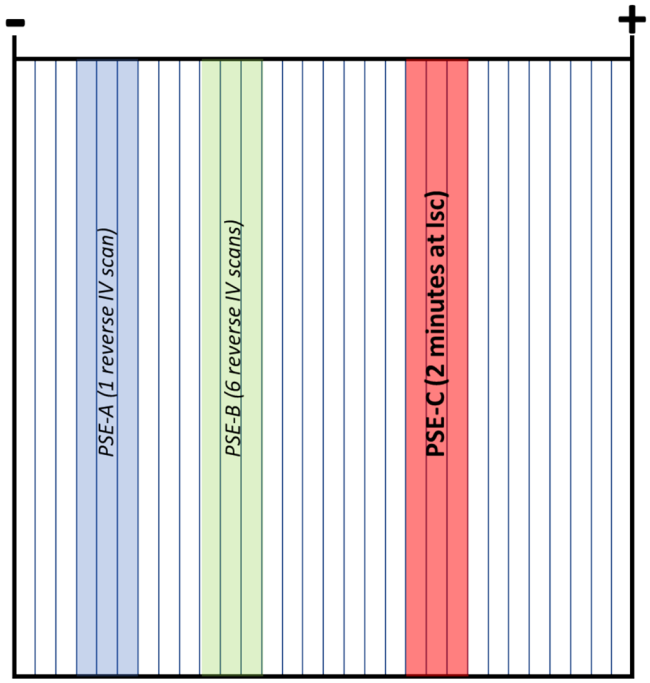

FIGURE 2 | Schematic of the module used for the partial shading experiments. The location of the three consecutive partial shading experiments, PSE-A, PSE-B, and PSE-C, is indicated.

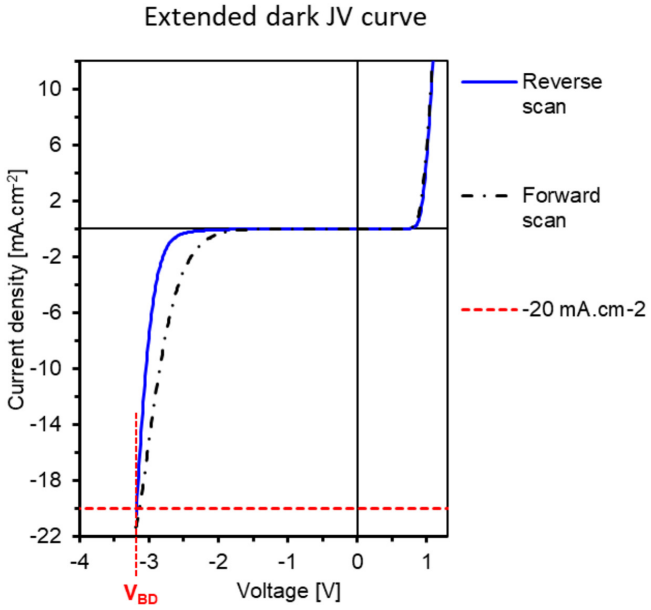

FIGURE 3 | Example of extended dark *JV* curve of individual cell used for V_{BD} determination. The dashed red line at $-20\,mA{\cdot}cm^{-2}$ is used to determine V_{BD}.

Figure 3. In the present study, the breakdown voltage is chosen as the voltage in the reverse scan (from positive to negative) yielding a current below $20\,mA{\cdot}cm^{-2}$ (dashed red line). This value was chosen because it is close to the typical J_{SC} expected in such devices.

3 | Results and Discussion

3.1 | Module Partial Shading

First, let us emphasize that the degradation observed after PSE-C (in *IV*, PL, and EL) is not isolated. It is very much consistent with the degradation induced by PSE-A and PSE-B in this module (see Figure S2) although those are not as strong as the effect of PSE-C. Other measurements not shown here, for example, on the module used to determine the optimum mask size, also show a similar impact of reverse bias exposure.

The effect of the partial shading experiment we focus on here, PSE-C, is shown in Figure 4, with the shaded area of PSE-C marked with red brackets. The corresponding *IV* parameters are shown in Table 1 (see also IV curves in Figure S3). The *IV* parameters after PSE-C show a 2.7% relative drop in efficiency (forward scan), driven mostly by a drop in fill factor. This modest degradation should be expected, since only three cells are effectively degraded out of the 31 interconnected cells in the module. In a real outdoor setting with shading elements in the surroundings, we expect that the repeated shading on various groups of cells will have a more detrimental impact on the *IV* parameters.

Luminescence techniques, on the other hand, do show significant alterations in the module. Indeed, the bottom part of the shaded area in Figure 4 (regions II and III) shows a higher PL signal at V_{OC} (c) and I_{SC} (e) than initially, but no signal in EL (d). EL requires the injected current to reach the semiconductor, which is clearly not possible in these regions of the shaded cells. The decreased luminescence in PL at I_{SC} (Figure 4e) indicates that the photogenerated carriers are not extracted by the electrodes. If the carriers were extracted as in the surrounding areas, the short circuit conditions should prevent all recombination in the perovskite stack itself, fully quenching the PL. Looking in more details, the PL signal at V_{OC} is brightest in region II and less bright in region III. We suspect non-radiative Shockley-Read-Hall recombination is occurring in region III, balancing out the more intense PL signal.

Additionally, non-radiative recombination can be observed in the ILIT image of Figure 4f. This thermogram shows local heating, predominately in region III of the shaded cells. It should be mentioned that ILIT was the first imaging technique applied after PSE-C, and the signal in region III became less intense during the measurement, indicating a fast partial recovery after initial degradation.

We note also that, contrary to the previous work mentioned in the introduction [14, 15], no shunting defects are formed in the present experiment.

Combining the data in Figure 4, we suggest that a potential barrier for the charge carriers is present at either (or both) perovskite interfaces. The effect of such a potential barrier at the perovskite-ETL interface on PL and EL signal intensity is illustrated in Figure 5, using quasi-Fermi level splitting (QFLS). In PL, the carrier extraction is prevented by the barrier, therefore, the amount of carriers recombining radiatively in the absorber (which relates to the QFLS) increases, thus boosting the PL intensity. In EL, on the other hand, the carrier injection is hindered by the barrier, thus decreasing the QFLS in the absorber and decreasing the EL intensity.

Several studies have reported on the possible formation of barriers induced by reverse bias exposure. Bowring et al. observed

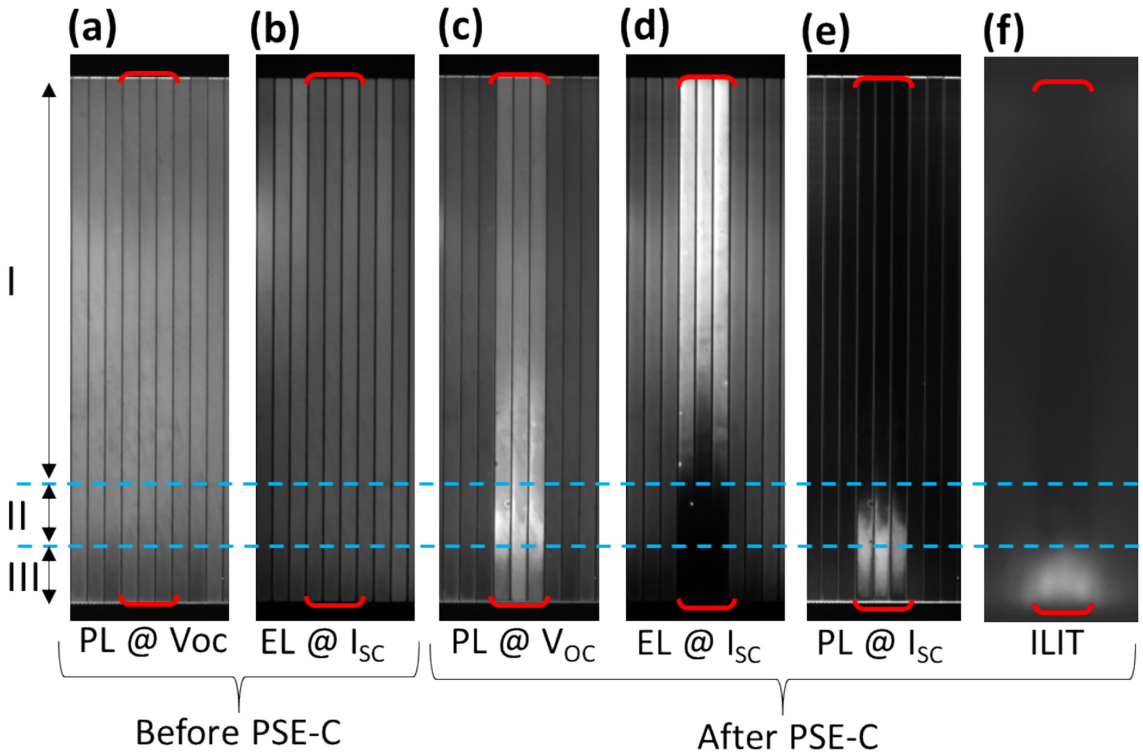

FIGURE 4 | (a) Photoluminescence and (b) electroluminescence before any partial shading. Characterization after PSE-C is also shown, with (c) the PL at V_{OC}, (d) the EL at I_{SC}, (e) the PL at I_{SC}, and (f) the ILIT images. The cells shaded in PSE-C are indicated in each image with a red bracket. Changes due to reverse bias exposure occurred in three distinct areas (I, II, and III), delineated in dashed blue. Note that these are cropped images highlighting the effect of PSE-C for better clarity of the figure. Full PL, EL, and ILIT images of the module can be found in Figure S2.

TABLE 1 | *IV* parameters of the module at three stages, initial, after PSE-B ("before PSE-C"), and after PSE-C.

	Forward scan				Backward scan			
	I_{SC} (mA)	V_{OC} (V)	FF (%)	PCE (%)	I_{SC} (mA)	V_{OC} (V)	FF (%)	PCE (%)
Initial	−60.2	34.5	70.1	14.5	−60.3	34.6	73.4	15.3
Before PSE-C	−58.8	34.6	68.0	13.8	−58.9	34.4	69.7	14.1
After PSE-C	−58.3	34.4	67.0	13.4	−58.4	34.2	68.3	13.6
Relative change before and after PSE-C (forward scan)	−0.8%	−0.5%	−1.4%	−2.7%	−0.8%	−0.6%	−2.1%	−3.5%

Note: The relative change in *IV* parameters induced by PSE-C (i.e., change between after PSE-B and after PSE-C) is also shown. The corresponding *IV* curves can be found in Figure S3.

an increase of the breakdown voltage and of the series resistance during/after the application of a reverse bias. Razera et al. detected iodine inside the organic ETL and reported the appearance of "s-shapes" (i.e., kinks) in *IV* curves after reverse bias degradation, which is usually associated with the presence of a potential barrier. This is also supported by other publications, where a similar barrier formation is observed [18, 19].

3.2 | Complementary Cell Characterization

To understand why reverse bias degradation occurs preferentially in one area of the module, we investigate individual cells ($4\times4\,mm^2$ area) with the same stack, slot-die coated on $6\times6\,in.^2$ substrates. Reverse bias degradation is thought to be current-driven. However, the breakdown voltage gives a good indication of the voltage at which currents flow. In this study, the breakdown voltage was defined as the applied reverse bias at which the cell current drops below $-20\,mA\cdot cm^{-2}$, which is close to J_{SC} at 1-sun illumination. A histogram of the breakdown voltage (V_{BD}) distribution across the sample is shown in Figure 6.

Although the V_{BD} distribution is close to a normal distribution (see dashed black line), it is rather wide, spanning between −2.3 and −4.1 V. Moreover, this variation in V_{BD} is not a gradual one, where, for example, the center of the sample would have uniform V_{BD} values, closer to the mean, gradually moving towards the tail values of the Gaussian distribution as we move towards the edges of the sample. Instead, we observe strong local fluctuations in V_{BD}, as illustrated in Figure 7.

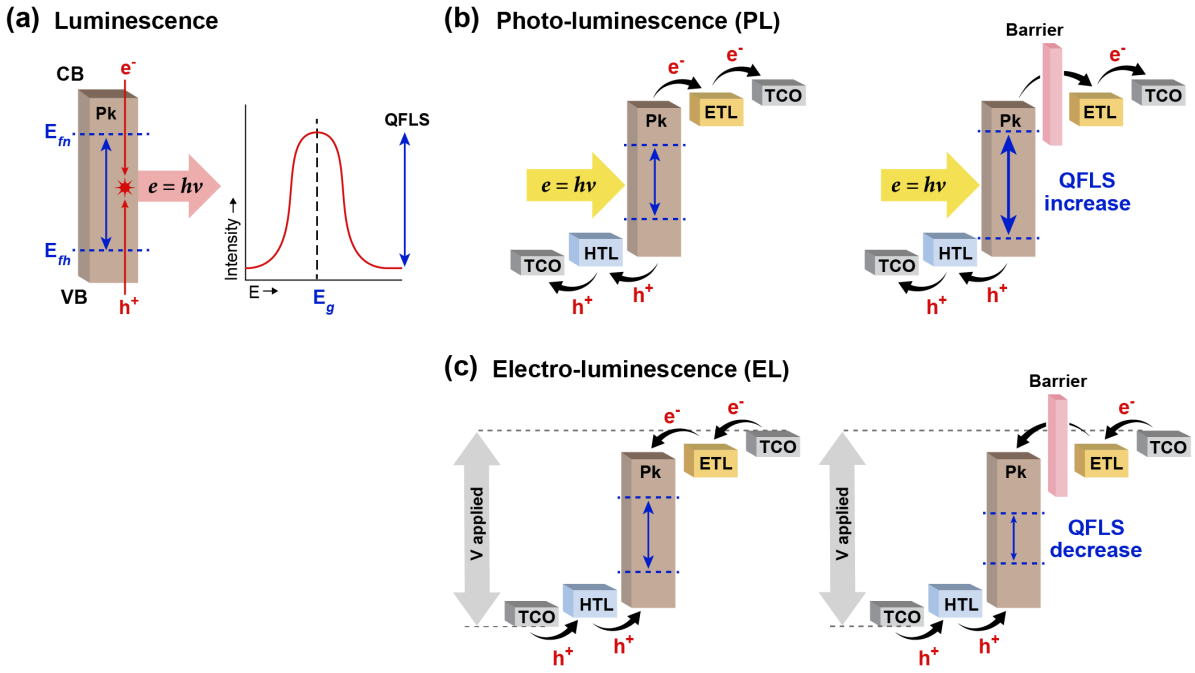

FIGURE 5 | Proposed mechanism behind the PL and EL behavior in the defective area. (a) The luminescence peak position of the absorber alone is defined by the bandgap, and its intensity by the quasi-fermi levels splitting (QFLS). If a barrier forms at one of the ETL interface, it will result, in PL, in the electrons being confined to the absorber instead of moving towards the electrodes, hence an increased PL intensity (b). In EL (c), on the other hand, the current injection to the absorber will be hindered resulting in less QFLS, that is, lower EL intensity.

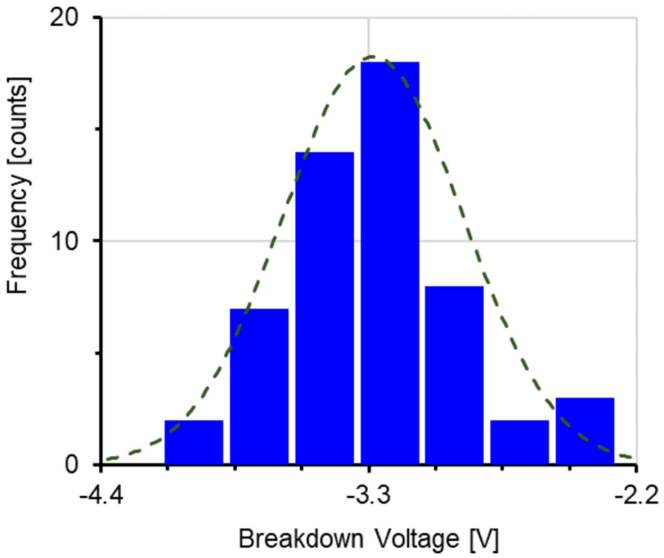

FIGURE 6 | Histogram of V_{BD} distribution (defined at $-20\,mA{\cdot}cm^{-2}$) in cells that are S2S deposited on a single $6\times6\,in.^2$ glass substrate. Under each bar, the range of V_{BD} values is indicated. The bar width represents the bin width. The dashed black line shows a normal distribution, based on the measured mean and standard deviation, for comparison.

Note that the PCE of the two cells shown in Figure 7 is similar, with 16.4% for cell 1 ($V_{BD}=-3.9\,V$) and 15.1% for cell 2 ($V_{BD}=-3.0\,V$). More generally, we do not observe a correlation between PCE and V_{BD}.

In Figure 7, we compare the *JV* curves of two neighboring cells, which were less than 3 cm apart (cell 1 in red, cell 2 in green). The ΔV_{BD} between these two adjacent cells is thus 1 V. Now, to relate this finding to the case of a module, let us picture the case where the areas of these two cells both belong to the same larger cell in a module: The resulting *JV* curve (black dashed line in (a)) can be approximated by a parallel connection between the two cells, as schematically illustrated in (b). This figure shows that at an equal voltage (−3.3 V dashed blue line) applied to the combined cell the resulting currents in the two regions are very different. In this example $20\,mA{\cdot}cm^{-2}$ passes through the combined cell, the bias currents of the individual regions represented by cells 1 and 2 are around −39.5 and $-0.5\,mA{\cdot}cm^{-2}$, respectively (see intercept of vertical dashed line). Note that this example is a simplified model of a cell (in a module) with non-uniform V_{BD}. We

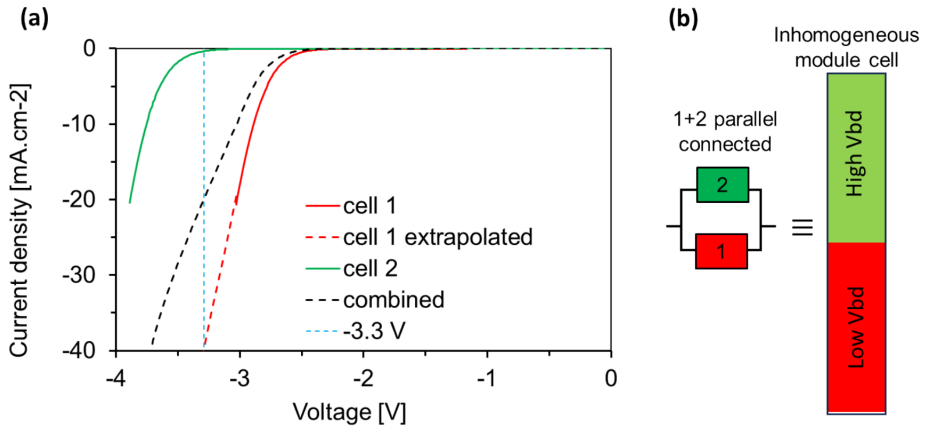

FIGURE 7 | (a) Reverse dark *JV* characteristics of two neighboring perovskite cells with similar efficiencies (red and green) and the calculated *JV* curve if these cells were both part of a larger cell in a module (modeled as a parallel connection in dashed black, with V_{BD} in dashed blue). Those cells were at two neighboring locations on the same 6 in.^{2} deposition plate. (b) Diagram illustrating the fact that two cells of different V_{BD} in parallel can model a module cell where the V_{BD} changes locally.

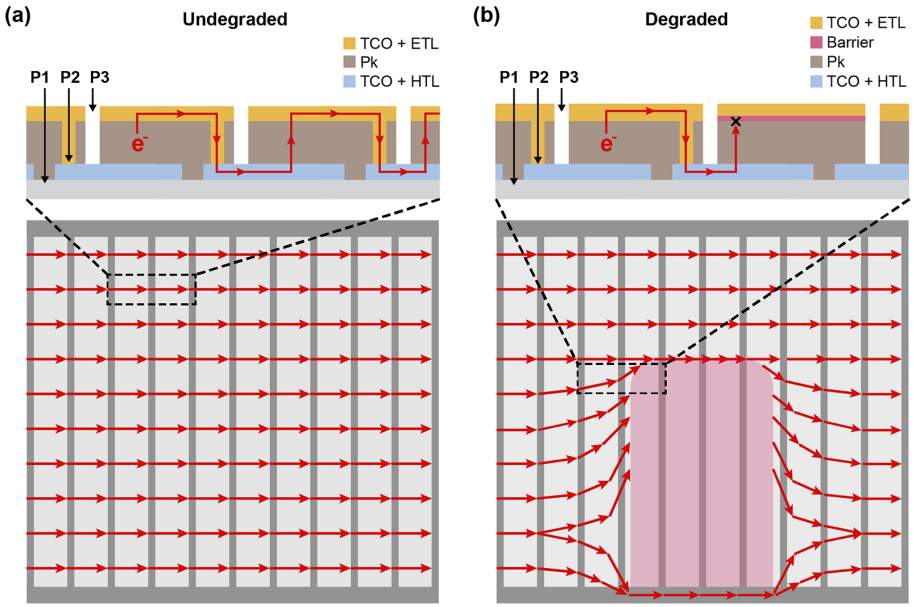

FIGURE 8 | Top view illustration of the likely current pathways during reverse bias in a module (a) without degraded area and (b) with a barrier at the perovskite/transport layer interface. Above each top view is a cross-sectional view, showing why the current cannot flow through the region with a potential barrier at the interface. A possible leakage current pathway at the bottom edge of the module is also depicted.

should also mention that the V_{BD} uniformity within the module might be better than in the sample with cells since the latter has more edges and interfaces, for example, due to overlapping TCO patterns.

3.3 | Proposed Degradation Mechanism in Partial Shading Degraded Modules

To explain the observations in regions I, II, and III, we suggest that areas with locally lower V_{BD} and/or higher current could be the starting points where the barrier forms, because higher currents will be passing through them than in higher V_{BD} areas. Once the barrier has formed at a low V_{BD} location, the current pathway will be diverted away. This is illustrated in Figure 8, where the current pathways around a region where the barrier has already formed are illustrated, along with cross-sectional views.

Since we observe barrier formation and increased non-radiative recombination in region III, which is located near the bottom edge of the module's active area, it is possible that the isolation scribe present at this location is partially responsible. However, a dedicated study would be necessary to determine whether this is indeed the case and what mechanism is involved.

4 | Conclusion

A perovskite module has been subjected to partial shading and shows signs of degradation as a result. We show that the intensity variation in PL at V_{OC} and J_{SC}, EL and ILIT imaging, all point

towards potential barrier formation at one of the perovskite/transport layer interfaces, preventing carrier extraction and injection. This result is consistent with mechanisms proposed in the literature at the individual cell level. In the present case, however, we are dealing with a monolithically interconnected module, which entails additional features. Since the cell areas are larger in a module, it leads to a wider breakdown voltage distribution (possibly due to material inhomogeneities) and higher currents passing in the low V_{BD} areas. The presence of scribes, such as an isolation scribe around the active area, can have an influence on the current flow during shading and thus on the formation of the interfacial layer, creating a potential barrier for the charge carriers. This is another feature that gives extra value to studying partial shading on modules rather than reverse bias on individual cells.

In summary, we show that opto-electronic imaging techniques can be combined in a non-destructive characterization protocol to draw meaningful conclusions on the degradation mechanism, their formation and propagation. They can also point to specific "weak spots" of the module to be studied in more detail with more precise (e.g., destructive) methods. Additionally, studying partial shading degradation at the module level reveals the more complex and realistic interplay between material and electrical parameters.

Author Contributions

Remi Aninat co-analyzed the results of the degradation experiments, co-selected the data, and led manuscript writing. Klaas Bakker led the design, execution, and analysis of the degradation experiments and co-wrote the manuscript. Jonathan Henzel led the literature review and the investigation into the degradation mechanism and reviewed the paper. Valerio Zardetto led the spin-coating and small cells fabrication (used, e.g., in Figure 6) and reviewed the paper. Ilker Dogan led the S2S Slot-die coating and monolithically interconnected module fabrication and reviewed the paper. Veronique Gevaerts led laser processing for monolithic interconnection and reviewed the paper. Sjoerd Veenstra acquired the funding for the module and cells manufacturing and reviewed the paper. Mirjam Theelen managed the project, joint results analysis, managed the financials, and reviewed the paper.

Acknowledgments

The authors acknowledge the assistance of Marcel Simor for the slot-die deposition and ITO deposition, Dorrit Roosen-Melsen for the encapsulation, Nadia Houtzager for the forward *JV* measurements of the individual cells, and Anne Biezemans for the laser interconnection.

Funding from the TNO knowledge investment project (KIP) is gratefully acknowledged.

Data Availability Statement

The data that support the findings of this study are available from the corresponding author upon reasonable request.

References

1. M. A. Green, E. D. Dunlop, M. Yoshita, et al., "Solar Cell Efficiency Tables (Version 63)," *Progress in Photovoltaics: Research and Applications* 32 (2024): 3–13.

2. A. Al-Ashouri, E. Köhnen, B. Li, et al., "Monolithic Perovskite/Silicon Tandem Solar Cell With >29% Efficiency by Enhanced Hole Extraction," *Science* 370 (2020): 1300–1309.

3. M. Jošt, E. Köhnen, A. Al-Ashouri, et al., "Perovskite/CIGS Tandem Solar Cells: From Certified 24.2% Toward 30% and Beyond," *ACS Energy Letters* 7 (2022): 1298–1307.

4. A. Rajagopal, Z. Yang, S. B. Jo, et al., "Highly Efficient Perovskite–Perovskite Tandem Solar Cells Reaching 80% of the Theoretical Limit in Photovoltage," *Advanced Materials* 29 (2017): 1702140.

5. I. Mathews, S. Sofia, E. Ma, et al., "Economically Sustainable Growth of Perovskite Photovoltaics Manufacturing," *Joule* 4 (2020): 822–839.

6. H. J. Snaith and P. Hacke, "Enabling Reliability Assessments of Pre-Commercial Perovskite Photovoltaics With Lessons Learned From Industrial Standards," *Nature Energy* 3 (2018): 459–465.

7. D. Lan and M. A. Green, "Combatting Temperature and Reverse-Bias Challenges Facing Perovskite Solar Cells," *Joule* 6 (2022): 1782–1797.

8. Y. Rong, Y. Hu, A. Mei, et al., "Challenges for Commercializing Perovskite Solar Cells," *Science* 361 (2018): eaat8235.

9. C. Wang, L. Huang, Y. Zhou, et al., "Perovskite Solar Cells in the Shadow: Understanding the Mechanism of Reverse-Bias Behavior Toward Suppressed Reverse-Bias Breakdown and Reverse-Bias Induced Degradation," *Advanced Energy Materials* 13 (2023): 2203596.

10. S. Baumann, G. E. Eperon, A. Virtuani, et al., "Stability and Reliability of Perovskite Containing Solar Cells and Modules: Degradation Mechanisms and Mitigation Strategies," *Energy & Environmental Science* 17 (2024): 7566–7599.

11. O. Breitenstein, J. Bauer, K. Bothe, et al., "Understanding Junction Breakdown in Multicrystalline Solar Cells," *Journal of Applied Physics* 109 (2011): 071101.

12. K. Bakker, J. Sala, M. Najafi, M. Daenen, and B. Geerligs, "Towards a Shade Tolerant Monolithically Interconnected Perovskite Module for Use in Four Terminal Tandem Devices," in *2022 IEEE 49th Photovoltaics Specialists Conference (PVSC)* (Philadelphia, PA: IEEE, 2022), 0748–0750, https://doi.org/10.1109/PVSC48317.2022.9938911.

13. S. M. Sze, Y. Li, and K. K. Ng, *Physics of Semiconductor Devices* (Hoboken, NJ: John Wiley & Sons, 2021).

14. A. R. Bowring, L. Bertoluzzi, B. C. O'Regan, and M. D. McGehee, "Reverse Bias Behavior of Halide Perovskite Solar Cells," *Advanced Energy Materials* 8 (2018): 1702365.

15. R. A. Razera, D. A. Jacobs, F. Fu, et al., "Instability of p–i–n Perovskite Solar Cells Under Reverse Bias," *Journal of Materials Chemistry A* 8 (2020): 242–250.

16. R. Aninat, K. Bakker, L. Jouard, M. G. Ott Cruz, P. Yilmaz, and M. Theelen, "Extraction and Microscopic Analysis of Partial Shading-Induced Defects in a Commercial CIGS PV Module," *Progress in Photovoltaics: Research and Applications* 30 (2022): 1101–1114.

17. K. Bakker, A. Weeber, and M. Theelen, "Reliability Implications of Partial Shading on CIGS Photovoltaic Devices: A Literature Review," *Journal of Materials Research* 34 (2019): 3977–3987.

18. I. E. Gould, C. Xiao, J. B. Patel, and M. D. McGehee, "In-Operando Characterization of P-I-N Perovskite Solar Cells Under Reverse Bias," in *2021 IEEE 48th Photovoltaic Specialists Conference (PVSC)* (Fort Lauderdale, FL: IEEE, 2021), 1365–1367, https://doi.org/10.1109/PVSC43889.2021.9518723.

19. L. Bertoluzzi, J. B. Patel, K. A. Bush, et al., "Incorporating Electrochemical Halide Oxidation Into Drift-Diffusion Models to Explain Performance Losses in Perovskite Solar Cells Under Prolonged Reverse Bias," *Advanced Energy Materials* 11 (2021): 2002614.

20. R. A. Kerner, Z. Xu, B. W. Larson, and B. P. Rand, "The Role of Halide Oxidation in Perovskite Halide Phase Separation," *Joule* 5 (2021): 2273–2295.

21. L. Geerligs, M. Najafi, K. Bakker, et al., *Reverse-Bias Studies of Semitransparent Perovskite Cells, and Model Evaluation of 4T Tandem Module Designs* (Milan: EUPVSEC, 2022).

22. J. Henzel, K. Bakker, M. Najafi, et al., "Impact of the Current on Reverse Bias Degradation of Perovskite Solar Cells," *ACS Applied Energy Materials* 6 (2023): 11429–11432.

23. S. Dongaonkar and M. A. Alam, "Geometrical Design of Thin Film Photovoltaic Modules for Improved Shade Tolerance and Performance," *Progress in Photovoltaics: Research and Applications* 23 (2015): 170–181.

24. W. Herrmann and M. Alonso, "Behaviour of Thin-Film Modules Under Shading," 19th EUPVSEC, Paris, 2004.

Supporting Information

Additional supporting information can be found online in the Supporting Information section.